

A versatile twin-microscope system for light-sheet imaging

A versatile twin-microscope system for light-sheet imaging

Kevin Keomanee-Dizon, Scott E. Fraser, and Thai V. Truong^{a)}

Translational Imaging Center, Viterbi School of Engineering, and Dornsife College of Letters, Arts and Sciences, University of Southern California, Los Angeles, CA 90089, USA

(Dated: 11 October 2019)

Recent developments in light-sheet microscopy techniques has led to its cutting-edge application across a range of fields, from developmental biology to behavioral neuroscience. Its low photodamage propensity allows biological dynamics to be imaged for a duration of several hours up to days; however, a tradeoff exists between such extended imaging sessions and imaging throughput, which in practice directly limits analysis workflows and the resulting time to biological discovery. Here, we present an economical instrument that can image multiple sample types simultaneously. Unlike any existing light-sheet microscope, our instrument, the flex-SPIM, shares both an ultrafast laser and a bank of continuous-wave lasers between two independently controlled light-sheet microscope-twins. Harnessing the power of modern lasers yields a substantial reduction in the cost of the light source over standard dual systems, and a doubling in imaging throughput relative to a single system. Each microscope-twin (i) operates in both one-photon and two-photon excitation modes, (ii) delivers one to three light-sheets *via* a trio of orthogonal excitation arms, (iii) provides sub-micron to micron imaging resolution, (iv) is multicolor compatible, and (v) permits upright and/or inverted light-sheet detection. We offer a detailed description of the flex-SPIM design to aid instrument builders who wish to construct and use a similar system. We then demonstrate the instrument's versatility for biological investigation by performing fast imaging of the beating heart in an intact zebrafish embryo, deep imaging of thick patient-derived tumor organoids, and gentle whole-brain imaging of neural activity in behaving larval zebrafish.

I. INTRODUCTION

Most of what we recognize as the phenomena of life are not properties of stationary structures, but rather emerge from dynamic interactions among many elements over time. Modern optical microscopy methods offer an efficient means for noninvasive, high-resolution observation and investigation of many of life's most fascinating phenomena. The difficulty is that tradeoffs must often be made between spatial resolution, acquisition speed, penetration depth, and the limited photon budget from the sample.¹ The last point is crucial to uncompromised biological imaging, as there are a finite number of photons that a given fluorophore can emit before its bleached, and high light doses on the specimen can lead to photo-induced toxicity. It is thus critical that light be used at low intensity and as efficiently as possible while striking the right balance of tradeoffs in performance for whatever the application demands.

In the past decade or so, there have been a series of important developments in light-sheet microscopy, a century-old technique² also known as selective-plane illumination microscopy (SPIM).³ SPIM decouples the illumination and detection paths: a cylindrical illumination lens is used to focus a static thin two-dimensional (2D) sheet of light orthogonal to the focal plane of a detection objective lens (Fig. 1). Whereas conventional point-scanning techniques acquire volumetric information one point at a time, light-sheet excitation provides rapid op-

tical sectioning of the three-dimensional (3D) sample volume (either by scanning the sample through the stationary light-sheet, or scanning the light-sheet through the stationary sample). The orthogonal geometry between the illumination and detection paths in combination with light-sheet excitation permits an entire 2D plane of fluorophores to be excited/detected with intrinsically high signal-to-noise ratios, high imaging speed, and minimal light exposure to the sample. Indeed, many recent developments in light-sheet microscopy techniques⁴⁻¹⁰ has led to its cutting-edge application across a range of fields,^{4-7,10,11} from developmental biology^{5,12} to behavioral neuroscience.^{10,11,13-15} Each of these techniques of course has its own tradeoffs in performance, the complexity and expense of the microscope optics, sample compatibility, as well as expenditure of the photon budget. Our goal here is describe key developments that motivate our instrument.

The first key development was to create light-sheets virtually with a focused Gaussian beam, generated *via* a low numerical aperture (NA) lens, and dynamically scanning it across the plane (Fig. 1).¹⁶ This virtually scanned light-sheet approach provides better spatial uniformity, higher light throughput, and more precise spatial control over the selected plane of interest compared to a static 2D light-sheet. For large-volume imaging, orthogonal excitation of the sample from multiple directions can additionally be employed to create a more uniform and larger illuminated plane.¹⁷

Two-photon light-sheet microscopy (2P-SPIM) was a further development, combining the high penetration depth of nonlinear excitation with the high speed and low photodamage associated with SPIM.¹⁸ The idea is that,

^{a)}Electronic mail: tvtruong@usc.edu.

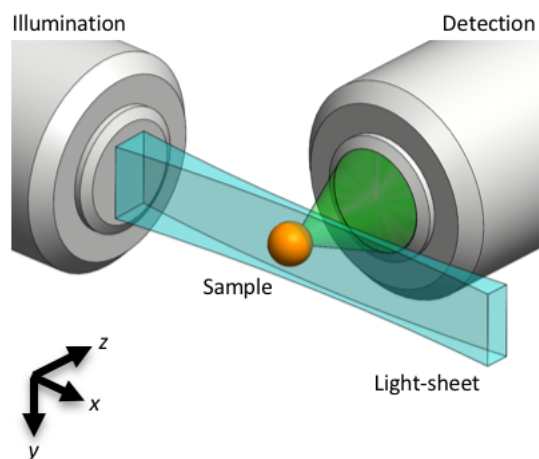


FIG. 1. Light-sheet microscopy principle. A static light-sheet (blue) can be created with a cylindrical lens. Alternatively the light-sheet can be formed dynamically by scanning a focused beam. The illuminated plane is detected (green) by an orthogonally positioned wide-field microscope. Axial sections are captured either by scanning the sample (orange) through the stationary focal plane, or by scanning the focal planes through the stationary sample.

compared with visible light, near-infrared (NIR) pulsed illumination minimizes the scattering-induced spatial degradation of the light-sheet over longer propagation distances, while the quadratic dependence of the 2P excited fluorescence signal on the excitation intensity reduces unwanted out-of-focus photons, both of which lead to improved axial resolution and contrast. The same low NA illumination lens used for 1P Gaussian light-sheet imaging can be utilized to generate an axially-extended focus of NIR femtosecond laser pulses for 2P light-sheet imaging, making it convenient to carry out both on the same setup.^{18,19} The 10-fold lower NA used for 2P light-sheet illumination generates orders of magnitude lower peak intensity for the same average excitation power compared to point-scanning 2P microscopy (2P-LSM); thus, nonlinear photodamage mechanisms are significantly reduced. In short, 2P-SPIM has proven successful in relatively thick or optically dense samples, imaging up to $2\times$ deeper than 1P-SPIM, and $> 10\times$ faster and with 100-fold lower peak intensity than with 2P-LSM.¹⁸ In the context of neuroscience, the NIR light used for 2P excitation is invisible to many animals, which avoids unintended visual stimulation.²⁰

The biggest drawback to 2P-SPIM is the requisite for an expensive ultrafast laser source. The high cost of an ultrafast pulsed laser and the reasonably complex assembly are both major barriers to the adoption of nonlinear SPIM for many laboratories, despite its superior performance in optically challenging samples. Even for laboratories that do have the means, in terms of both budget and expertise, the ultrafast source is likely tied to a single microscope. As the photon budget sets the upper limit on how much excitation energy can be delivered to the

sample, these implementations typically waste $>$ half of the total laser power available.

Part and parcel with the photon budget, the low photodamage propensity of SPIM permits biological processes to be imaged for a duration of several hours up to days. Unfortunately, a tradeoff exists between such prolonged imaging sessions and imaging throughput, which in practice directly limits analysis workflows and the resulting time to biological discovery. There is thus substantial motivation for a light-sheet instrument that efficiently uses of the high-power capabilities of modern laser sources and can also image multiple samples. Ideally, such an instrument should be easily adaptable to different applications and the associated sample properties. Here we describe an instrument designed and built to meet these aims.

Unlike any existing light-sheet microscope, our instrument, the flex-SPIM, shares both an ultrafast laser and a bank of continuous-wave lasers between two independently controlled light-sheet microscope-twins. This yields a substantial reduction in the cost of the light source over standard dual systems, and a doubling in imaging throughput relative to a single system. By combining and improving a series of unique developments, some introduced earlier in this section, each microscope-twin has built-in modularity for tailoring around a diverse class of samples and scientific questions. In the following section we describe the flex-SPIM design in detail, for optical physicists or engineers who wish to construct and use a similar instrument. We then showcase its utility by characterizing the system and performing imaging of the beating larval zebrafish heart and patient-derived tumor organoids. Throughout, we demonstrate the ease of integrating auxiliary elements to adapt the flex-SPIM to meet specific sample needs: optimizing our instrument to observe the neural dynamics that drive behavior in the zebrafish, which enables us to extend the depth of 2P functional imaging to the whole brain with uncompromised spatiotemporal resolution.

II. INSTRUMENT DESIGN

The flex-SPIM draws on important lessons taken from the arduous challenges posed by going from proof-of-principle studies^{18,19} with a new imaging technology to meaningful scientific results.^{21–23} Several years of interactions between the 2P-SPIM inventors and end users at advanced imaging centers (at the California Institute of Technology and University of Southern California) resulted in the flex-SPIM: a photon-efficient SPIM instrument that can image multiple sample types simultaneously. The flex-SPIM is conceptually similar to our earlier 2P-SPIM setup (see Refs. 18 and 19), but functionally distinct *via* the following combination of improvements. First, two independent microscope-twins share the light source (Fig. 2). We reasoned that the high-power of modern lasers provided an opportunity to share

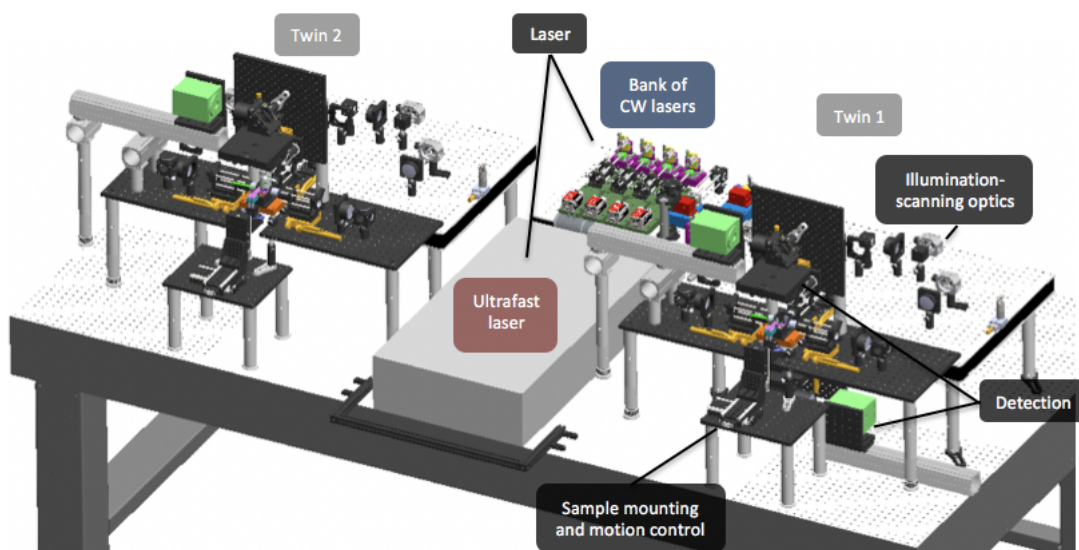


FIG. 2. 3D opto-mechanical model of the twin-microscope system mounted on a 5 foot \times 10 foot, anti-vibration optical table. Model shows the laser subsystem shared between microscope-twin-1 (right) and microscope-twin-2 (left). Twin-1 has the four functional subsystems labeled and features an implementation of both upright and inverted light-sheet detection.

TABLE I. flex-SPIM functional subsystems and modules. CW: continuous-wave; polarization optics: half-wave plate and polarizing beamsplitter; AOTF: acousto-optic tunable filter; LED: light-emitting diode

Subsystem/module	Description	Main components ^a
Laser	Laser modulation and beam routing	CW lasers; beam expander; dichroic mirrors; polarization optics; AOTFs; mirrors Ultrafast laser; polarization optics; beam expander; Pockels cells; mirrors
Illumination-scanning optics	Generating the light-sheet	Scanning optics; objective lenses; mirrors
Detection	Image formation	Scientific camera; tube lens; filter wheel; filters; objective
Sample mounting and motion control	Holding and imaging the 3D sample	Custom sample chamber/holder; motion stages; piezoelectric z-stage
Instrument control	Control and timing of components	Acquisition computer; National Instruments PXI; system mainframe and scaling amplifiers
Auxiliary	Zebrafish eye masks and tail channel	Camera; LED; filter; aluminum masks

^a The main parts for each subsystem and module used to build the flex-SPIM are listed in Table SI.

both a bank of CW lasers and an ultrafast laser between two light-sheet microscopes; this would allow us to simultaneously achieve three goals: (i) economical use of the most typically expensive component of advanced light microscopes—the laser source; (ii) a dramatic reduction in the cost of two microscopes; and (iii) an increase in both 1P- and 2P-SPIM imaging throughput compared to a single microscope. To our knowledge, no light-sheet dual/twin system sharing the same light source has been demonstrated.

Second, the system is “flexible” in the sense that the opto-mechanical design is open and modular (Fig. 2, 3, and 4), providing a straight-forward path to instrument evolution and customization for different samples and applications (Fig. 5). Switching from high spatial resolution (sub-micron) to a lower spatial resolution (micron) with a larger field of view, for example in Fig. 7 and 8, is

relatively simple and only requires modification to the detection subsystem. Third, to further accommodate a diversity of specimens, the flex-SPIM can be configured in an upright and/or inverted light-sheet detection geometry (Fig. 2). Finally, we also added a trio of excitation objectives mounted orthogonally (Fig. 3), to enhance illumination uniformity and increase optical coverage for large and opaque samples. Other design refinements that result in improved performance are detailed in the following subsections.

The entire dual/twin system sits on a 5 foot \times 10 foot, anti-vibration optical table. The instrument consists of four functional subsystems (Fig. 2) and two modules (Table I). The schematic diagram of the integrated illumination paths is shown in Fig. 3 and the corresponding 3D opto-mechanical model is shown in Fig. 2. Whenever possible, commercially available hardware components are

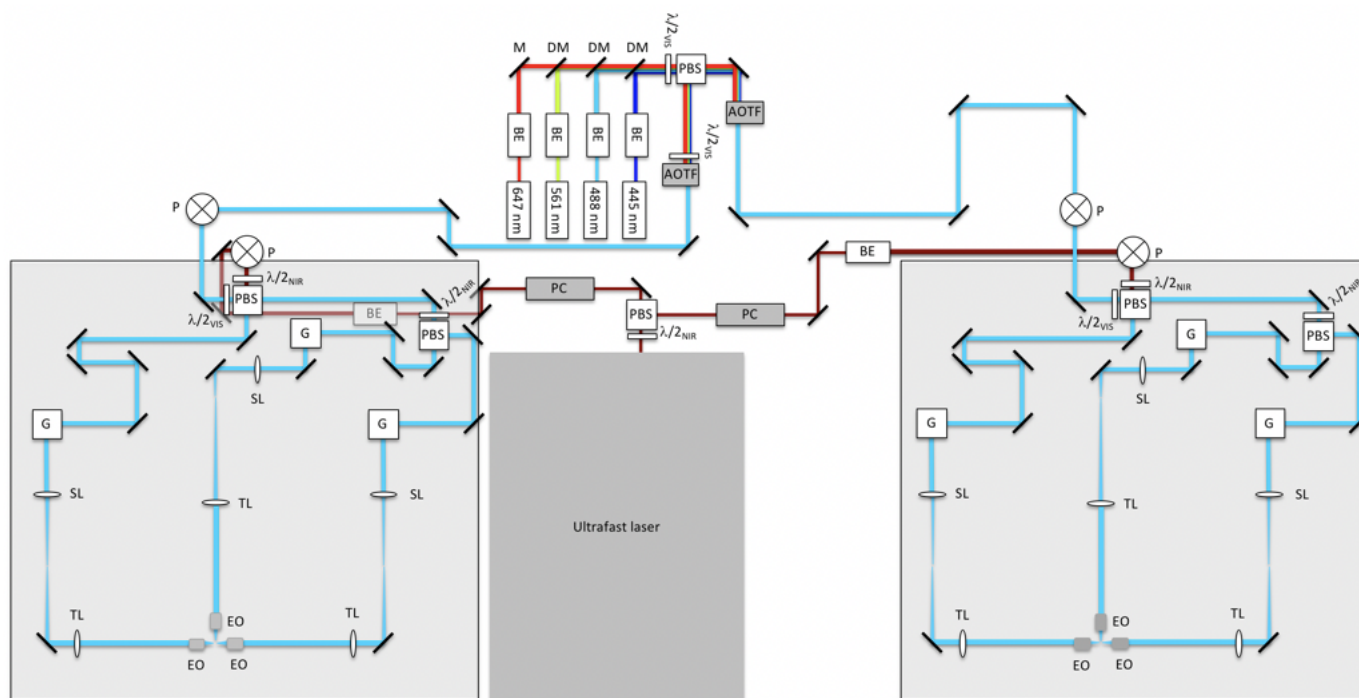


FIG. 3. Schematic diagram of laser and illumination-scanning optics subsystems of the instrument. BE: beam expander; M: mirror; DM: dichroic mirror; $\lambda/2$: half-wave plate mounted in a rotation mount, where the subscripts VIS and NIR refer to the visible and near-infrared wavelengths, respectively; PBS: polarizing beamsplitter; AOTF: acousto-optic tunable filter; PC: Pockels cell; P: periscope; G: 2D scanning galvo mirrors; SL: scan lens; TL: tube lens; EO: excitation objective.

used; however, both basic machining of off-the-shelf parts and fabrication of custom components are required (Table SI). Most standard optical elements are mounted in Thorlabs 30 mm or 60 mm cage components. Beam steering mirrors shared by both the ultrafast and CW lasers (illumination-scanning optics) have protected silver coatings, whereas those used by the ultrafast or CW lasers alone have broadband dielectric coatings. System light throughput is sufficient for both the ultrafast and CW laser sources to simultaneously run both twins—two experiments in parallel—using the same (or different) wavelength(s).

A. Laser subsystem

Visible light from a bank of CW lasers at 445 nm, 488 nm, 561 nm, and 647 nm are collimated and expanded to a $1/e^2$ diameter of 2.5 mm before being combined into a co-linear beam using broadband and dichroic mirrors. (see Table SI)²⁴ The combined beam is then split into two paths of equal length and power through polarization optics (consisting of a half-wave plate mounted in a rotation mount and polarizing beamsplitter), delivering light to each microscope-twin. Note here that the linear polarizations of the beams for the twin-1 path and the twin-2 path now differ from each other. Each light path passes through acousto-optic tunable filters (AOTFs), which are

used to select the wavelengths and adjust the power independently for each twin. The AOTFs we use (Table SI) require a particular input polarization to maximize the diffraction efficiency and ensure chromatic co-linearity of the modulated beam, that is, the AOTF requires the input laser beam polarization to be linear orthogonal with respect to the baseplate (s-polarization). To match this requirement in the twin-1 path, the AOTF is mounted so that the crystal output face is used as the 'input' face, *i.e.*, the p-polarized beam enters the AOTF through its output face. The twin-2 path passes through a half-wave plate to rotate their polarization for maximum diffraction efficiency by the AOTF (Fig. 3). The AOTF in the twin-2 path is mounted conventionally. The CW lasers are used for single- or multi-color imaging *via* linear excitation.

Tunable NIR light from a mode-locked laser is split into two paths of equal length and power through polarization optics, delivering NIR light to each microscope-twin. Note here that again the linear polarizations of the beams for the twin-1 path and the twin-2 path now differ. Each path passes through a Pockels cell to adjust the power independently for each twin (Fig. 3). Similar to the AOTF, the Pockels requires a particular input polarization to maximize the extinction ratio and transmit near-minimum with 0 volts DC bias; as such, each Pockels is rotated with respect to the beam's input polarization to match this requirement. Following the Pockels for each path, the beams are expanded to a $1/e^2$ diam-

eter of 2.4 mm. The tunable NIR ultrafast laser is used for single- or multi-color imaging *via* nonlinear excitation. For nonlinear excitation at wavelengths > 800 nm, a long-pass filter is mounted upstream of the polarization optics to block any undesired residual wavelengths from the ultrafast laser.

B. Illumination-scanning optics subsystem

Visible and NIR beams from the laser subsystem are each raised onto a 24 inch \times 36 inch optical breadboard by periscopes (Fig. 3). The visible and NIR beams are combined into a co-linear beam *via* polarization optics, which also serves to split the combined beam into two paths (illumination arms 1 and 2) of equal length. Visible and NIR half-wave plates, which are each mounted in manual rotation mounts, rotate their polarization for *desired* transmission into illumination arms 1 and 2. Illumination arm 1 is further split into two paths through polarization optics, creating a total of 3 illumination arms, again of equal path lengths. The NIR half-wave plate can be used to further adjust the transmission into illumination arms 1 and 3 (Fig. 3).

The beams from each illumination arm are sent to 2D scanning galvanometer (galvo) mirror positioning systems. The first galvo mirror rapidly scans the beam laterally to synthesize the light-sheet (in the x - y plane), and the second galvo mirror, which is conjugate to the back pupil of the excitation objective lens, scans the virtual light-sheet along the (z) detection axis. Following the scanning system, each illumination beam passes through a scan lens (achromatic doublet; see Supplementary Note 1); a tube lens; and a low magnification, low NA, long-working-distance excitation objective lens. All the distances between any pair of these lenses forms a $4f$ arrangement, *i.e.*, the distance between any pair of lenses is equal to sum of their focal lengths.

Three excitation objective lenses are mounted orthogonal to each other, and direct the illumination light toward the sample (Fig. 3). Depending on the sample properties, any combination of the excitation objectives can be used, either sequentially or simultaneously. Small and/or transparent samples, for example, may benefit from single-sided illumination with linear excitation. Whereas relatively large and thick samples may benefit from the uniform illumination coverage offered by using all three objectives with nonlinear excitation.

Both the 1P and 2P Gaussian-beam light-sheets are ~ 10 μm in average thickness across a length of ~ 400 μm , as shown in Fig. 7(d), yielding an effective (x - y) field-of-view of $\sim 400 \times 1000$ μm^2 . These parameters correspond to an illumination NA of ~ 0.02 and ~ 0.03 for 1P and 2P, respectively. This design choice was motivated by our desire to resolve single neurons ($6 - 8$ μm in size) throughout the entire $\sim 400 \times 800 \times 250$ μm^3 brain of zebrafish larva at 7 days-post-fertilization (dpf).^{20,25}

Since the signal rate is generally lower when operating

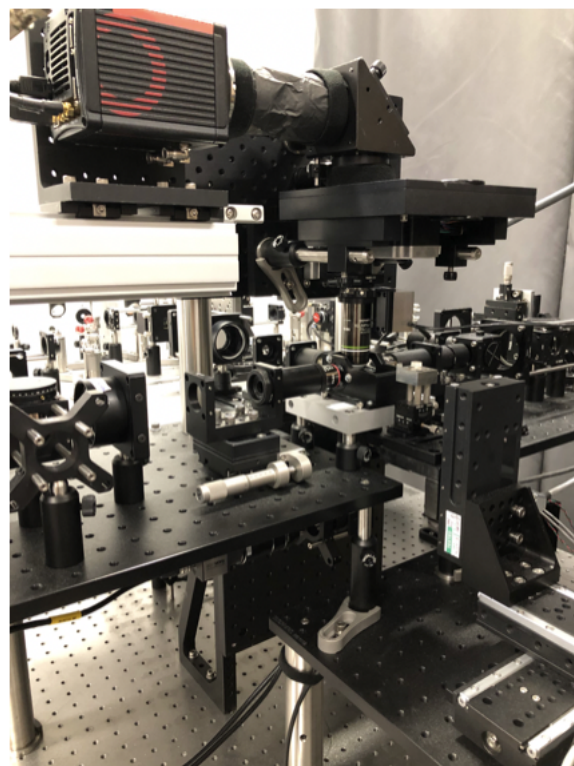


FIG. 4. Photograph of an assembled microscope-twin.

in the 2P excitation regime, we optimized most of the illumination-scanning optics for NIR wavelengths (Table SI). We define system throughput for each twin as the total measured laser power at the sample from the 3 illumination arms divided by the measured laser power at the laser source. At $\lambda = 900$ nm, system throughput for twin-1 and twin-2 are $\sim 55\%$ and $\sim 70\%$, respectively; thus, the overall throughput from the ultrafast laser to the sample is $> 60\%$ (summed average for both twins). System throughput in the visible regime was taken by throughput measurements across each CW laser line. As such, system throughput for twin-1 and twin-2 are $\sim 2\%$ and $\sim 10\%$, respectively; thus, the overall throughput from the CW laser bank to the sample is $\sim 10\%$ (summed average for both twins). This throughput is sufficient for both the ultrafast and CW laser sources to simultaneously run experiments on both twins using the same (or different) wavelength(s).

C. Detection subsystem

The sheet of fluorescence signal generated at the sample is collected by an orthogonally positioned water-immersion detection objective lens ($20\times$, NA = 1.0), which is mounted to a piezoelectric (piezo) collar. The high NA detection not only enables high-resolution imaging but also maximizes light-collection efficiency, which is important to minimize photodamage of the live sam-

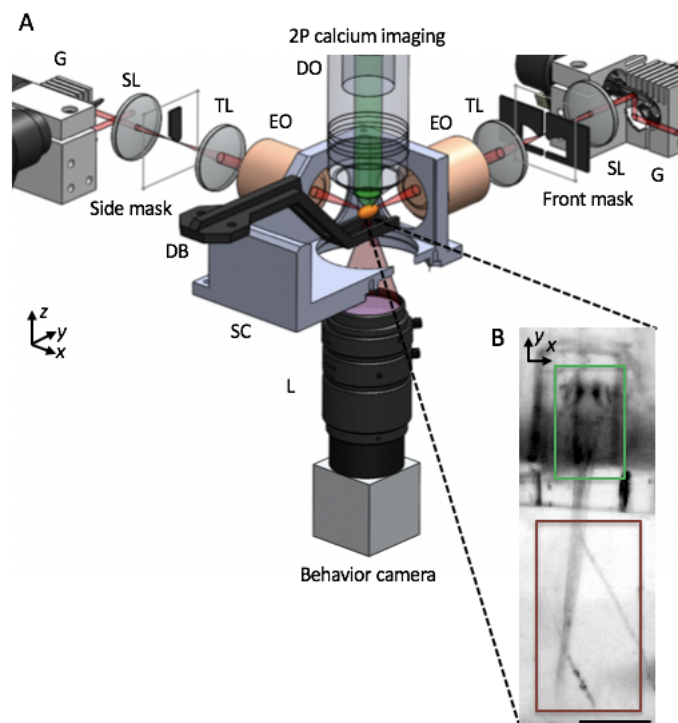


FIG. 5. (A) Schematic of apparatus for gentle imaging of neural activity during various behaviors in the larval zebrafish. Sheets of laser light are synthesized by quickly scanning the illumination beam (red) with galvo mirrors (G), and the agarose-embedded head of the animal is then illuminated with excitation objectives (EO) from the side and front arms. The side masks cover each eye on the sides of a horizontally oriented zebrafish, while the front mask covers both eyes, enabling access to neurons between the eyes. 2P-excited calcium fluorescence signal is collected through an upright detection objective (DO) and onto a scientific CMOS camera. A triggerable wide-field camera is positioned below the sample chamber (SC) to provide a wide-field, low-resolution view of the sample, as shown in (B). During a typical neural imaging experiment, the zebrafish's head is immobilized in agarose while the tail is free, thereby enabling us to monitor zebrafish behavior through tail movement. SL: scan lens; TL: tube lens; DB: dive bar; SC: sample chamber; L: camera lens. The third illumination arm, emission filter, detection TL, scientific camera, LED, and filter for behavior channel are not shown. Insets in (B) highlight that the calcium fluorescence channel (green) is recorded from the zebrafish brain, while the behavioral channel (dark red) monitors the tail movement of the animal. Scale bar, (B) 400 μm .

ples. The fluorescence signal passes through a filter wheel equipped with emission filters to block the excitation light and transmit the fluorescence signal emitted by the sample; the emission filters are optimized for CFP, GFP, mCherry, and Cy5, as well as other fluorophores with similar spectral characteristics (see Table SI). A tube lens then forms the primary image of the fluorescence signal onto a scientific complementary metal-oxide-semiconductor (sCMOS) camera.

Depending on the sample properties, the detection subsystem can be setup in upright and/or inverted configurations. For the tests presented here, we have primarily employed an upright configuration, as shown in Fig. 4, that is optimized for imaging neural activity in behaving larval zebrafish (Fig. 5). Switching to an inverted light-sheet detection geometry, or changing the overall magnification is relatively straight-forward, owing to the system's arrangement of opto-mechanical components in space (Fig. 2, 3, and 4). By mounting the camera on a rail (Fig. 2 and 4), the camera itself is designed to be conveniently adjusted, so that tube lenses of different focal lengths can be used to provide different magnifications.

D. Sample mounting and motion control subsystem

The custom sample chamber has three side windows for the excitation objectives as well as a bottom window to provide an additional view of the specimen. The sample chamber is open at the top, and is filled with imaging buffer; the open-top allows the detection objective to be liquid-immersed and the custom sample holder to be inserted. The sample chamber sits on a custom heat exchanger that has circulatory channels for temperature regulated fluid flow, which can be used to keep the medium-filled sample chamber at a specific temperature.

The sample holder is comprised of a caddy that holds the specimen, and a dive bar that holds the caddy. Caddies can be used for general agarose embedding of the sample or adapted to specific applications. For example, we have designed a caddy to image neural activity in behaving zebrafish, such as in Fig. 5(b), where the specimen's head is immobilized with 1.5% low-melting agarose gel (to record neural activity), while the tail is free to move (to record swimming behavior). The dive bar is mounted to a dual-axis goniometer, providing rotational motions around the x - and y -axis; the goniometer is mounted to a motorized 3D stack-up of linear stages (see Table SI), with each stage providing ± 25 mm of travel range. The combination of the two-axis goniometer and 3D stage stack-up allows fine sample positioning so that the region of interest can be readily overlapped with the detection objective focal plane. Again, depending on the sample properties and scientific question, a modified sample holder and/or chamber may be fabricated and used.

The flex-SPIM has two different modes of capturing volumetric information from a 3D sample: either by sample-scanning or objective-scanning. In both implementations, all the microscope objectives share a common focal point and volumes are acquired plane-wise at different axial positions.

In the sample-scanning mode, the sample is moved *via* the z -stage of the 3D stage stack-up along the optical axis of the detection subsystem and, while the excitation light-sheet and detection objective remain stationary, image stacks are sequentially collected. This approach is

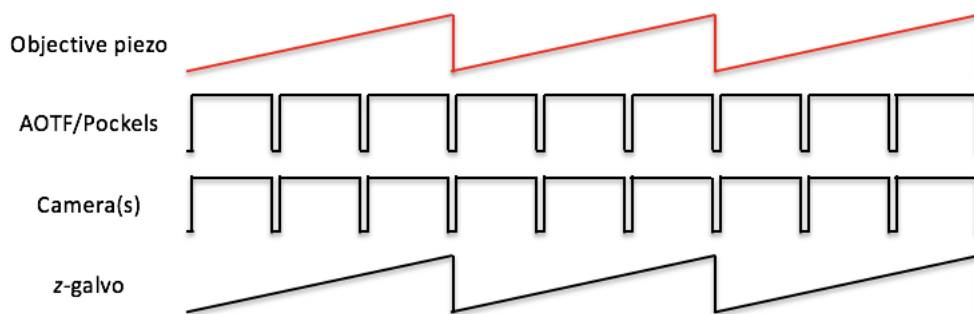


FIG. 6. Schematic of control signal sequences for objective-scanning mode. The position of the objective piezo collar is used as the master timing signal to generate control signals for the AOTF/Pockels, imaging cameras (both the scientific camera and behavior camera), and z -galvos. The number of pulses driving the AOTF/Pockels and cameras, shown as 3 in the schematic here, determine the number of individual z -plane images to be recorded during a single z -scan cycle over the sample.

the simplest to implement in practice, but its imaging speed is limited by mechanical inertia and the translational motion of the specimen can compromise normal biology.

In the objective-scanning mode, the movement of the detection objective piezo collar is synchronized with the second galvo mirror of each illumination arm: both the light-sheet and piezo collar are scanned axially, with a travel range of $\pm 500\mu\text{m}$ set by the piezo collar, during which image stacks are sequentially collected. This approach enables fast volumetric imaging without moving the specimen, and is preferred for our whole-brain functional imaging and simultaneous behavioral observation studies with zebrafish.

E. Instrument control module

Each twin is independently controlled with a Supermicro computer equipped with two Xeon E5-2650 v4 processors and 128 GB of 2400 MHz DDR4 RAM; and seven PCIe slots, enough space for all the control cards. While most of the instrument control and image acquisition routines are done through Micro-Manager,²⁷ custom software developed in LabVIEW (National Instruments) is used to independently control each of the 2D scanning galvo mirror systems, and allows precise alignment (size and swept-rate control) of the excitation light-sheet relative to the sample. Collected images are written directly to a dual-disk array consisting of eight 7200 RPM, 4 TB disks during imaging.

In the objective-scanning mode, the piezo collar's controller is used as the master timing source. The analog position-readout of the piezo collar triggers a PicoScope, which is used to generate control signal sequences to synchronize the AOTF or Pockels and camera(s) with image capture. The position-readout of the piezo collar is also used to drive the position of the z -galvos. Analog control signals for the galvos and AOTF or Pockels are appropriately scaled by individual scaling amplifiers. A schematic of the control signal sequences is shown in

(Fig. 6).

F. Auxiliary module

To avoid illumination of the zebrafish eyes while imaging neural activity, excitation light is physically blocked with a pair of masks for each side of a horizontally positioned zebrafish, and a mask for the front that covers both eyes [Fig. 5(a)]. These masks, fabricated out of black anodized aluminum, are mounted at the image planes of the illumination-scanning optics, each on a 2D translational stage to allow accurate positioning for different fish, or removal for non-neuro applications. A far-red light-emitting diode and a wide-field camera, positioned to view the sample from the bottom, enable view-finding and monitoring the tail behavior during neural imaging of the zebrafish (Fig. 5).

III. INSTRUMENT PERFORMANCE

We characterize the 3D resolution of the flex-SPIM by measuring the point spread function (PSF) with sub-diffraction fluorescent beads. We then demonstrate the utility of the instrument for investigating biological systems by imaging the beating embryonic zebrafish heart, thick patient-derived tumor organoids, and neural activity in behaving zebrafish.

A. Resolution characterization

We empirically measure the system PSF with sub-diffraction (175 ± 5 nm diameter) fluorescent beads (PS-Speck Microscope Point Source Kit, P7220, Molecular Probes) embedded in 1.5% agarose. Using PSFj,²⁶ we compute an averaged PSF from > 10 individual bead sub-volumes imaged at $44\times$ magnification. The averaged lateral and axial FWHM \pm SD values are: 1P, 500 nm ± 55 nm and $2.1 \mu\text{m} \pm 470$ nm, respectively; and 2P, 540

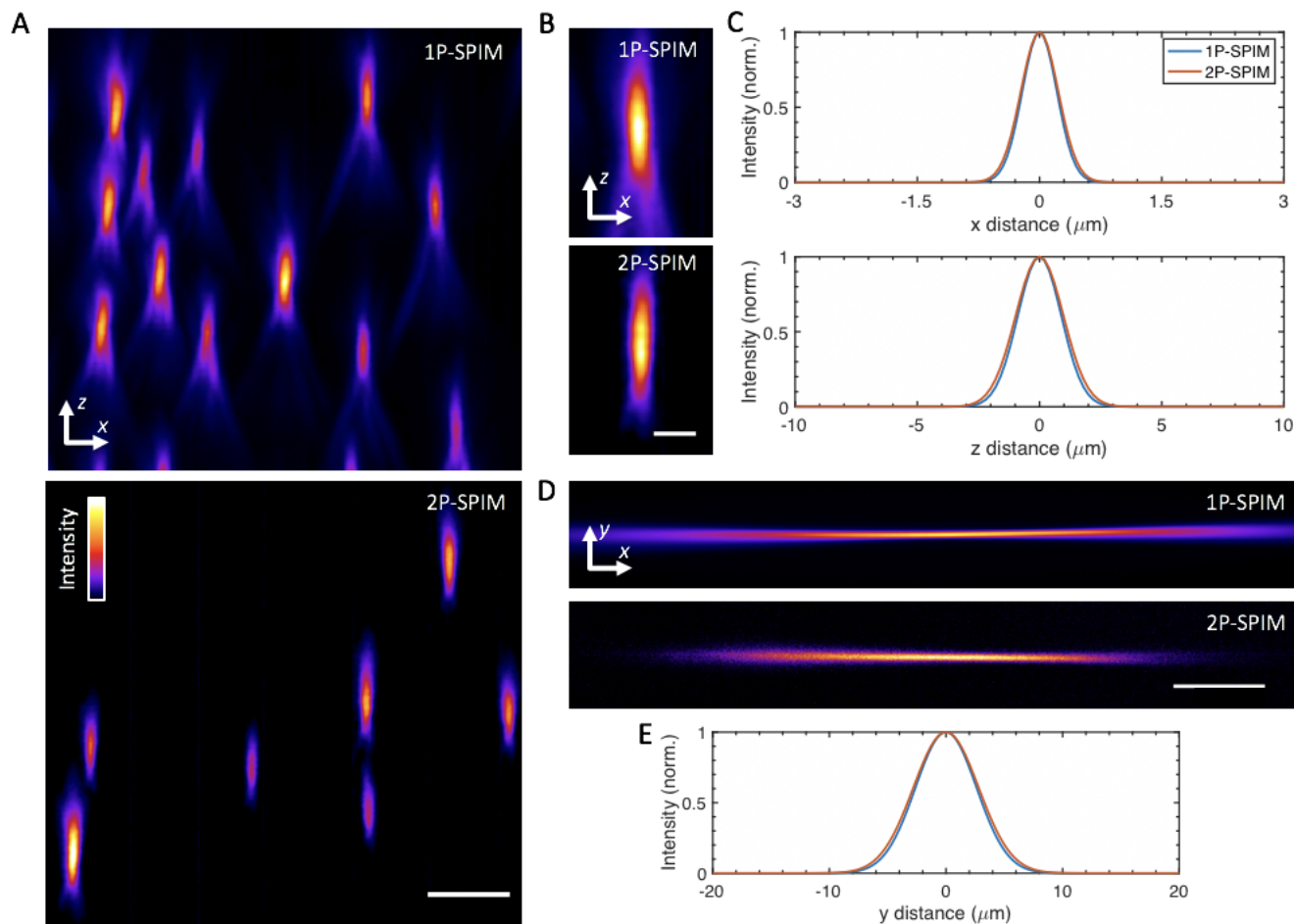


FIG. 7. System imaging performance and characterization. (A) y maximum-intensity projections of agarose-embedded 175 nm fluorescent beads imaged at $44\times$ magnification, in 1P (top) and 2P excitation mode (bottom). A false-color (fire) look-up table was used to enhance visualization. (B) Selected y maximum-intensity projections of sub-diffraction fluorescent beads, in 1P (top) and 2P mode (bottom). (C) Averaged lateral (top) and axial (bottom) full-width at half-maximum (FWHM) extents for the imaged beads, determined by fits of > 10 bead intensity profiles using PSFj.²⁶ Averaged lateral and axial FWHM \pm SD values are: 1P, $500 \text{ nm} \pm 55 \text{ nm}$ and $2.1 \mu\text{m} \pm 470 \text{ nm}$, respectively; and 2P, $540 \text{ nm} \pm 70 \text{ nm}$ and $2.3 \mu\text{m} \pm 370 \text{ nm}$, respectively. (D) Experimental images of fluorescence excited by 1P (top) and 2P (bottom) Gaussian focused beams, which are scanned in the y direction to create virtual light-sheets. Images were acquired by illuminating a solution of fluorescein in the sample chamber. (E) Intensity line profiles for the focused beams in (D), taken at the center of focus, with approximate values: 1P, $6.2 \mu\text{m}$; and 2P, $6.6 \mu\text{m}$. These FWHM values yield an averaged light-sheet thickness of $\sim 10 \mu\text{m}$ across the $400 \mu\text{m}$ extent along the x direction, centered around the Gaussian focus. Scale bars, (A) $5 \mu\text{m}$, (B) $2.5 \mu\text{m}$, (D) $150 \mu\text{m}$.

$\text{nm} \pm 70 \text{ nm}$ and $2.3 \mu\text{m} \pm 370 \text{ nm}$, respectively. Both the lateral and axial PSFs are larger than the theoretical diffraction-limited performance by $\sim 40 - 50\%$ for two primary reasons. First, our detection optical aperture is limited by the aperture of our filter wheel (see Table SI), which is smaller than the full aperture of the detection objective. Second, the effective pixel size at the camera was 146 nm at $44\times$ magnification, which was slightly larger than the Nyquist limit of $\lambda_{\text{det}}/(4\text{NA}_{\text{det}}) = 129 \text{ nm}$, so spatial sampling was insufficient to exploit the full detection NA. Despite these practical limitations, the flex-SPIM is still able to achieve sub-micron, subcellular lateral resolution in both 1P and 2P mode, as shown in Fig. 7(c) and 8. Representative bead images are shown in

Fig. 7(a) and (b). Excitation wavelengths were set to 488 nm and 920 nm for 1P- and 2P-SPIM, respectively, with the wavelength of emitted fluorescence centered at 515 nm.

B. Light-sheet imaging of the beating zebrafish heart

We demonstrate the performance of single-plane illumination with the flex-SPIM by capturing the dynamic motion of the beating heart in a 5-dpf transgenic larval zebrafish with the vasculature fluorescently labeled. A 1P excitation ($\lambda = 488 \text{ nm}$) light-sheet was parked in z to optically section through the heart of the agarose-

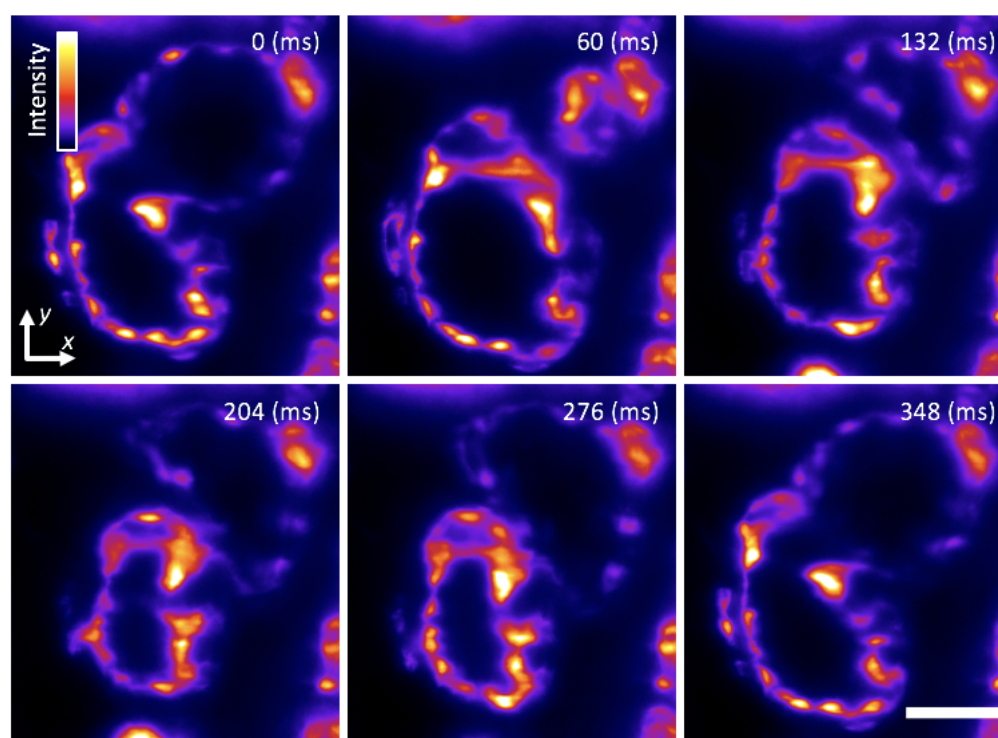


FIG. 8. Single-plane SPIM recording of the beating heart in a live 5-dpf larval zebrafish with the endocardium fluorescently labeled (GFP), showing 6 distinct time points during the cardiac beating cycle. A false-color (fire) look-up table was used to enhance visualization. Frames were captured with a magnification of $11\times$ and 5 ms exposure time, at a rate of 85 framers per second. Movie S1 shows a movie of the same data. Scale bar, $50\ \mu\text{m}$.

embedded sample, as we rapidly acquired images of the beating motion of the heart at 85 frames per second with subcellular resolution (Fig. 8 and Movie S1).

C. 3D imaging of thick, patient-derived tumor organoids

3D cell culture systems, such as spheroids or organoids, recapitulate the native physiology of multicellular tissues much better than 2D culture systems.²⁸ In the context of cancer, multicellular organoids permit the study of disease development and patient-specific response to therapy.²⁹ Unfortunately, these multicellular systems are scattering and aberrating, and are thus challenging to image with conventional instruments. To show the advantages of the flex-SPIM for such opaque and optically heterogenous samples, we imaged chemically fixed, agarose-embedded organoids differentiated from a patient with colorectal cancer that transgenically express nuclear-localized H2B-GFP [Fig. 9(a) and Movie S2]. In this thick scattering sample, the 2P excitation regime reduces the background haze [Fig. 9(b-c)] and provides better contrast throughout the imaged volume compared to 1P-excitation [Fig. 9(e)]. This is due to the reduced scattering of the longer excitation wavelength ($\lambda = 900\ \text{nm}$) of 2P excitation, which enables better-preserved light-sheet shape over longer propagation dis-

tances. Further, even when the excitation light scatters, the fluorescence signal is still spatially restricted mainly to the central part of the light-sheet (where intensity is the highest) because of the quadratic dependence of the 2P-excited fluorescence signal on the excitation intensity. Thus, by mitigating the scattering-induced thickening of the light-sheet, 2P excitation reveals more clearly-resolved cells than 1P deep in the sample [Fig. 9(d) and (f)].

D. Whole-brain functional imaging of behaving zebrafish

In larval zebrafish with genetically encoded calcium indicators, SPIM enables recording simultaneously the activity of many individual neurons across the entire brain.^{13,14} These implementations, however, likely stimulate the blue photoreceptors and other photosensitive cells in the fish retina with the visible excitation wavelengths used during light-sheet acquisition. Such illumination can reduce visual sensitivity to stimuli and interfere with visually driven processes.²⁰ NIR ($\lambda = 930\ \text{nm}$) 2P-SPIM overcomes this photostimulation problem,²⁰ achieving a recording depth of $120\ \mu\text{m}$ (sampled by 9 z -planes) at a 1 Hz volume rate.¹⁵ We push the depth of 2P SPIM neural functional imaging further with the flex-SPIM: more than doubling the volume size

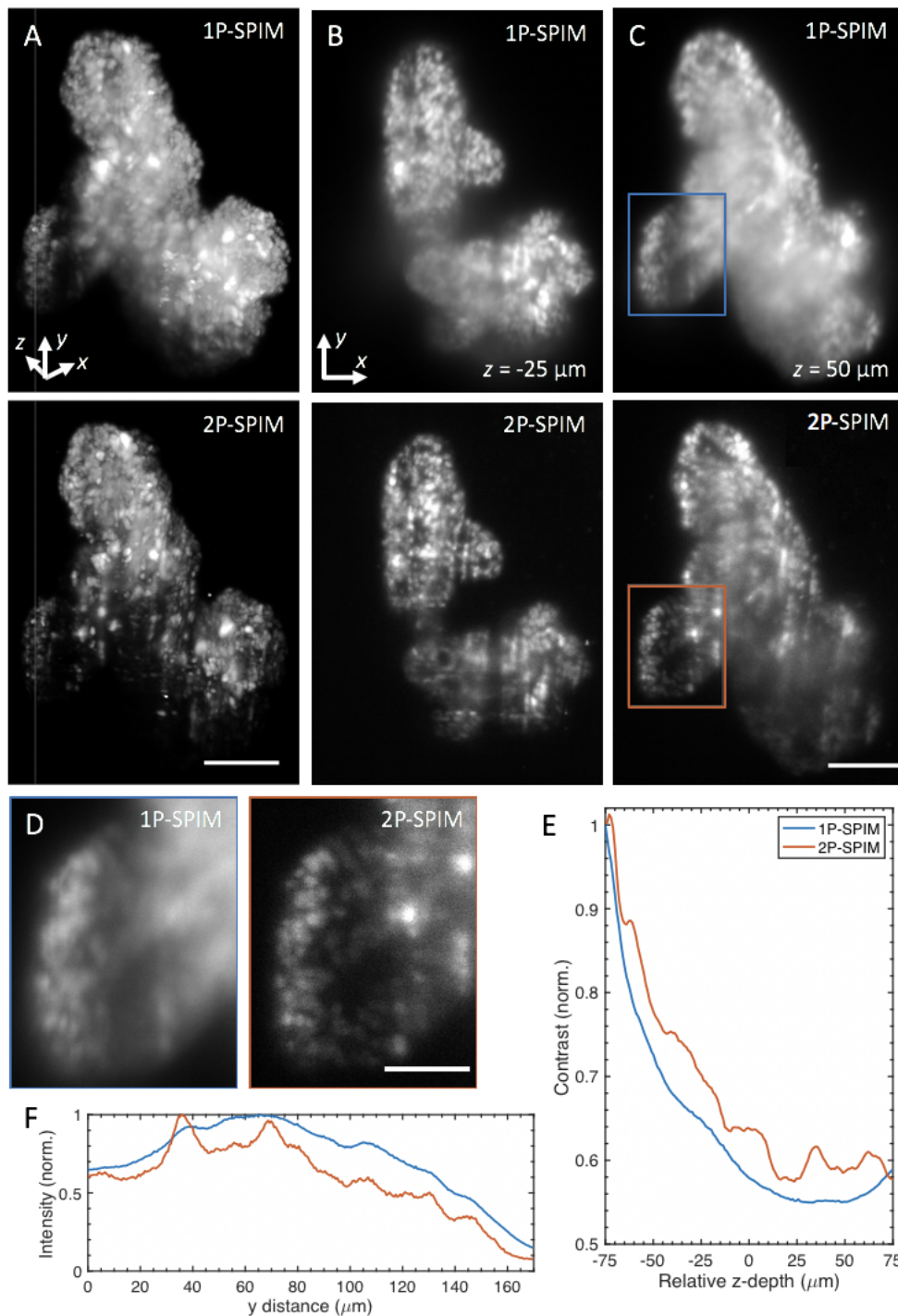


FIG. 9. One- and two-photon (1P, 2P) SPIM imaging of thick tumor organoids derived from a patient with colorectal cancer. (A) Volume rendering of fixed patient-derived tumor organoids expressing nuclear-localized H2B-GFP recorded in 1P (top) and 2P mode (bottom). 3D organoid captured with a magnification of $11\times$ and a volume of $\sim 400 \times 550 \times 150$ (x - y - z) μm^3 , with $1\text{-}\mu\text{m}$ z -steps and 150 ms exposure time. Movie S2 rotates the 3D-rendered volume of the same datasets. (B) and (C) are x - y image slices of (A) at $z = -25 \mu\text{m}$ ($50 \mu\text{m}$ from the surface) and $z = 50 \mu\text{m}$ ($125 \mu\text{m}$ from the surface), respectively. (D) Magnified images of the boxed regions in (C), for 1P (left) and 2P (right) mode. (E) Quantification of image contrast as a function of z -depth, calculated from the standard deviation of the pixel intensities from each x - y image slice and then normalized by the corresponding average image intensity. Each slice (from both modalities) is normalized against the surface slice ($z = -75 \mu\text{m}$) of 1P-SPIM. (F) Sum intensity along the x direction of images in (D) as a function of light-sheet propagation distance y . In both intensity profiles, intensity values were normalized by the global maximum. Scale bars, (A, C) $100 \mu\text{m}$, (D) $50 \mu\text{m}$.

while maintaining high spatiotemporal performance, as shown in Fig. 10 and Movie S3. By employing a trio of 2P excitation arms with masks at the image planes to avoid direct laser illumination to the eyes, we are able to image the entire volume of the brain of a 7-dpf larval zebrafish expressing the calcium indicator H2B-GCaMP6. We achieve a volume coverage of $400 \times 800 \times 250$ (x - y - z) μm^3 (sampled by 52 z -planes) at a 0.5 Hz volume rate with single-cell resolution, while simultaneously monitoring swimming behavior with a wide-field camera (Fig. 5). The total average laser power delivered to the sample from the three illumination arms was 490 mW in the objective-scanning mode for several minutes with no apparent phototoxicity. We went further to assess whether this excitation dosage was tolerable by exposing the animal for 11 hours, and observed no change in the calcium dynamics or any phenotypic signs of phototoxicity.

IV. CONCLUSION

An instrument with two independently controlled light-sheet microscope-twins sharing the same light source has been designed and presented. The design makes economical use of the power of modern lasers, dramatically reducing the cost of two microscopes, and increasing the imaging throughput compared to a single scope, which is particularly important for systematic and quantitative studies of biological processes that occur over many hours or days. Each twin provides sample flexibility through operation in both 1P and 2P excitation modes, the delivery of one to three light-sheets *via* a trio of orthogonal excitation arms, sub-micron to micron imaging resolution, multicolor compatibility, and built-in modularity to tailor the instrument around a specific sample and scientific question, all of which are often not easily done on a comparable, single system. We demonstrate the utility of the instrument by rapid single-plane imaging of the beating heart in a living zebrafish embryo. We also image patient-derived tumor organoids, and show the superior performance of 2P over 1P excitation in this relatively large and opaque sample. By optimizing the flex-SPIM for investigating the neural dynamics that drive behavior in larval zebrafish, we more than double the depth-coverage of 2P functional whole-brain light-sheet imaging without comprising spatiotemporal resolution. The flex-SPIM instrument can be replicated as described, or modified and further optimized. For example, the AOTF and/or Pockels cell can be used to generate intensity-modulated illumination patterns for incoherent structured-illumination to enhance the contrast in more scattering specimens.³⁰ Live organoid imaging is another example. Since 3D cell culture systems demand special environmental conditions to survive, successful modification of the instrument would require designing a new sample chamber rig with both temperature and CO₂ control, in which plane-wise detection is likely done in an inverted geometry.

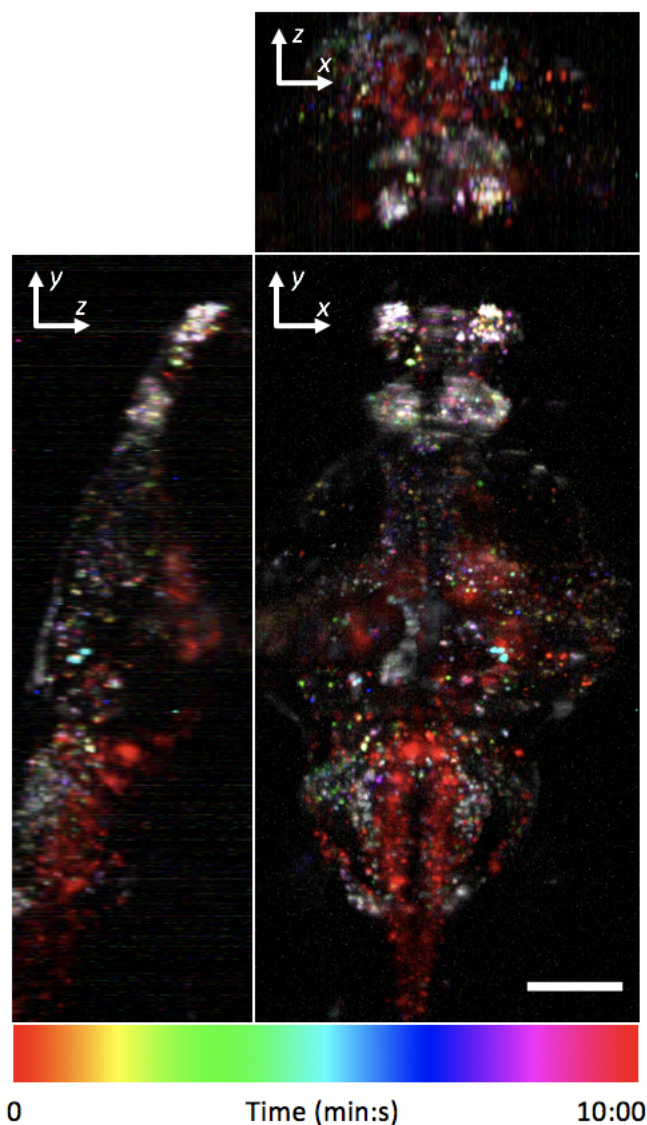


FIG. 10. Whole-brain functional imaging in behaving 7-dpf transgenic larval zebrafish expressing nuclear-localized H2B-GCaMP6S. Maximum-intensity projections of calcium activity are color-coded in time over the 10-minute recording window. Active neurons that exhibit fluorescence change during the recording appear as colored dots. Volume of $400 \times 800 \times 250$ (x - y - z) μm^3 is sampled by 52 z -planes ($4.8 \mu\text{m}$ z -steps) at 0.5 Hz with $11\times$ magnification. Movie S3 shows a 3D rendered movie of the same data. Scale bar, $100 \mu\text{m}$.

Appendix: Supplementary material

See supplementary material for a detailed list of the main flex-SPIM parts (Table SI), 1P-SPIM imaging of the beating embryonic zebrafish heart (Movie S1), a volume rendering of patient-derived tumor organoids (Movie S2), a 2P-SPIM recording of neural activity in a behaving animal (Movie S3), and simulations of scan lens performance (Supplementary Note 1).

ACKNOWLEDGMENTS

We are grateful to Sara Madaan for custom LabView software; Matt Jones for electronics help; Peter Luu for zebrafish sample preparations; Seungil Kim and Shannon Mumenthaler (Lawrence J. Ellison Institute for Transformative Medicine of USC) for providing the organoid samples; and Jon Daniels (Applied Scientific Instruments, Inc.) for valuable thoughts on beam-scanning in light-sheet microscopy. Special thanks to Andrey Andreev and the other members of the Translational Imaging Center for insightful discussions, and staff at the Viterbi/Dornsife Machine Shop for technical assistance. This work was supported in part by the National Institutes of Health (1R01MH107238-01), the Human Frontier Science Program (53-4895-008), and the USC-Olympus Innovation Partnership in Multiscale Bioimaging. K. Keomanee-Dizon was supported in part by the Alfred E. Mann Doctoral Fellowship.

- ¹J. Vermot, S. Fraser, and M. Liebling, *HFSP Journal* **2**, 143 (2008).
- ²H. Siedentopf and R. Zsigmondy, *Annalen Der Physik* **10**, 1 (1902).
- ³J. Huisken, J. Swoger, F. D. Bene, J. Wittbrodt, and E. Stelzer, *Science* **305**, 1007 (2004).
- ⁴L. Gao, L. Shao, B. C. Chen, and E. Betzig, *Nature Protocols* **9**, 1083 (2014).
- ⁵R. M. Power and J. Huisken, *Nature Methods* **14**, 360 (2017).
- ⁶A. K. Glaser, N. P. Reder, Y. Chen, E. F. McCarty, C. Yin, L. Wei, Y. Wang, L. D. True, and Y. T. C. Liu, *Nature Biomedical Engineering* **1**, 0084 (2017).
- ⁷T. L. Liu, S. Upadhyayula, D. E. Milkie, V. Singh, K. Wang, I. A. Swinburne, K. R. Mosaliganti, Z. M. Collins, T. W. Hiscock, J. Shea, A. Q. Kohrman, T. N. Medwig, D. Dambournet, R. Forster, B. Cunniff, Y. Ruan, H. Yashiro, S. Scholpp, E. M. Meyerowitz, D. Hockemeyer, D. G. Drubin, B. L. Martin, D. Q. Matus, M. Koyama, S. G. Megason, T. Kirchhausen, and E. Betzig, *Science* **360**, eaaq1392 (2018).
- ⁸M. Kumar, S. Kishore, J. N. D. L. McLean, and Y. Kozorovitskiy, *Optics Express* **26**, 13027 (2018).
- ⁹B. Yang, X. Chen, Y. Wang, S. Feng, V. Pessino, N. Stuurman, N. H. Cho, K. W. Cheng, S. J. Lord, L. Xu, D. Xie, R. D. Mullins, M. D. Leonetti, and B. Huang, *Nature Methods* **16**, 501 (2019).
- ¹⁰V. Voleti, K. B. Patel, W. Li, C. P. Campos, S. Bharadwaj, H. Yu, C. Ford, M. J. Casper, R. W. Yan, W. Liang, C. Wen, K. D. Kimura, K. L. Targoff, and E. M. C. Hillman, *Nature Methods* **16**, 1054 (2019).
- ¹¹E. M. C. Hillman, V. Voleti, W. Li, and H. Yu, *Annual Review of Neuroscience* **42**, 295 (2019).
- ¹²K. McDole, L. Guignard, F. Amat, A. Berger, G. Malandain, L. A. Royer, S. C. Turaga, K. Branson, and P. J. Keller, *Cell* **175**, 859 (2018).
- ¹³M. B. Ahrens, M. B. Orger, D. N. Robson, J. M. Li, and P. J. Keller, *Nature Methods* **10**, 413 (2013).
- ¹⁴N. Vladimirov, Y. Mu, T. Kawashima, D. V. Bennett, C. T. Yang, L. L. Looger, P. J. Keller, J. Freeman, and M. B. Ahrens, *Nature Methods* **11**, 883 (2014).
- ¹⁵S. Wolf, A. M. Dubreuil, T. Bertoni, U. L. Böhm, V. Bornmuth, R. Candelier, S. Karpenk, D. G. Hildebrand, I. H. Bianco, R. Monasson, and G. Debrégeas, *Nature Communications* **8**, 651 (2017).
- ¹⁶P. J. Keller, A. D. Schmidt, J. Wittbrodt, and E. H. K. Stelzer, *Science* **322**, 1065 (2008).
- ¹⁷J. Huisken and D. Stainier, *Optics Letters* **32**, 2068 (2007).
- ¹⁸T. V. Truong, W. Supatto, D. S. Koos, J. M. Choi, and S. E. Fraser, *Nature Methods* **8**, 757 (2011).
- ¹⁹V. Trivedi, T. V. Truong, L. A. Trinh, D. B. Holland, M. Liebling, and S. E. Fraser, *Biomedical Optics Express* **6**, 2056 (2015).
- ²⁰S. Wolf, W. Supatto, G. Debrégeas, P. Mahou, S. Kruglik, J. M. Sintes, E. Beaurepaire, and R. Candelier, *Nature Methods* **12**, 370 (2015).
- ²¹G. T. Reeves, N. Trisnadi, T. V. Truong, M. Nahmad, S. Katz, and A. Stathopoulos, *Developmental Cell* **22**, 544 (2012).
- ²²D. V. Bower, N. Lansdale, S. Navarro, T. V. Truong, D. J. Bower, N. C. Featherstone, M. G. Connell, D. A. Alam, M. R. Frey, L. A. Trinh, G. E. Fernandez, D. Warburton, S. E. Fraser, D. Bennett, and E. C. Jesudason, *Biology Open* **6**, 1458 (2017).
- ²³D. A. Lee, A. Andreev, T. V. Truong, A. Chen, A. J. Hill, G. Oikonomou, U. Pham, Y. K. Hong, S. Tran, L. Glass, V. Sapin, J. Engle, S. E. Fraser, and D. A. Prober, *Elife* **6**, e25727 (2017).
- ²⁴B. C. Chen, W. R. Legant, K. Wang, L. Shao, D. E. Milkie, E. Daniel, M. W. Davidson, W. Michael, C. Janetopoulos, X. S. Wu, J. A. Hammer, Z. Liu, B. P. English, Y. Mimori-Kiyosue, D. P. Romero, A. T. Ritter, J. Lippincott-Schwartz, L. Fritz-Laylin, R. D. Mullins, D. M. Mitchell, J. N. Bembenek, A. C. Reyman, R. Böhme, S. W. Grill, J. T. Wang, G. Seydoux, U. S. Tulu, D. P. Kiehart, and E. Betzig, *Science* **346**, 1257998 (2014).
- ²⁵E. A. Naumann, A. R. Kampff, D. A. Prober, A. F. Schier, and F. Engert, *Nature Communications* **13**, 513 (2010).
- ²⁶P. Theer, C. Mongis, and M. Knop, *Nature Methods* **11**, 981 (2014).
- ²⁷A. D. Edelstein, M. A. Tsuchida, N. Amodaj, H. Pinkard, R. D. Vale, and N. Stuurman, *Journal of Biological Methods* **1** (2015).
- ²⁸F. S. and A. Schmitz and E. H. K. Stelzer, *Nature Protocols* **12**, 1103 (2017).
- ²⁹T. Takahashi, *Annual Review of Pharmacology and Toxicology* **59**, 447 (2019).
- ³⁰P. J. Keller, A. D. Schmidt, A. Santella, K. Khairy, Z. Bao, J. Wittbrodt, and E. H. K. Stelzer, *Nature Methods* **7**, 637 (2010).
- ³¹B. Schmid, P. Tripal, T. Fraaß, C. Kersten, B. Ruder, A. Grüneboom, J. Huisken, and R. Palmisano, *Nature Methods* **16**, 278 (2019).